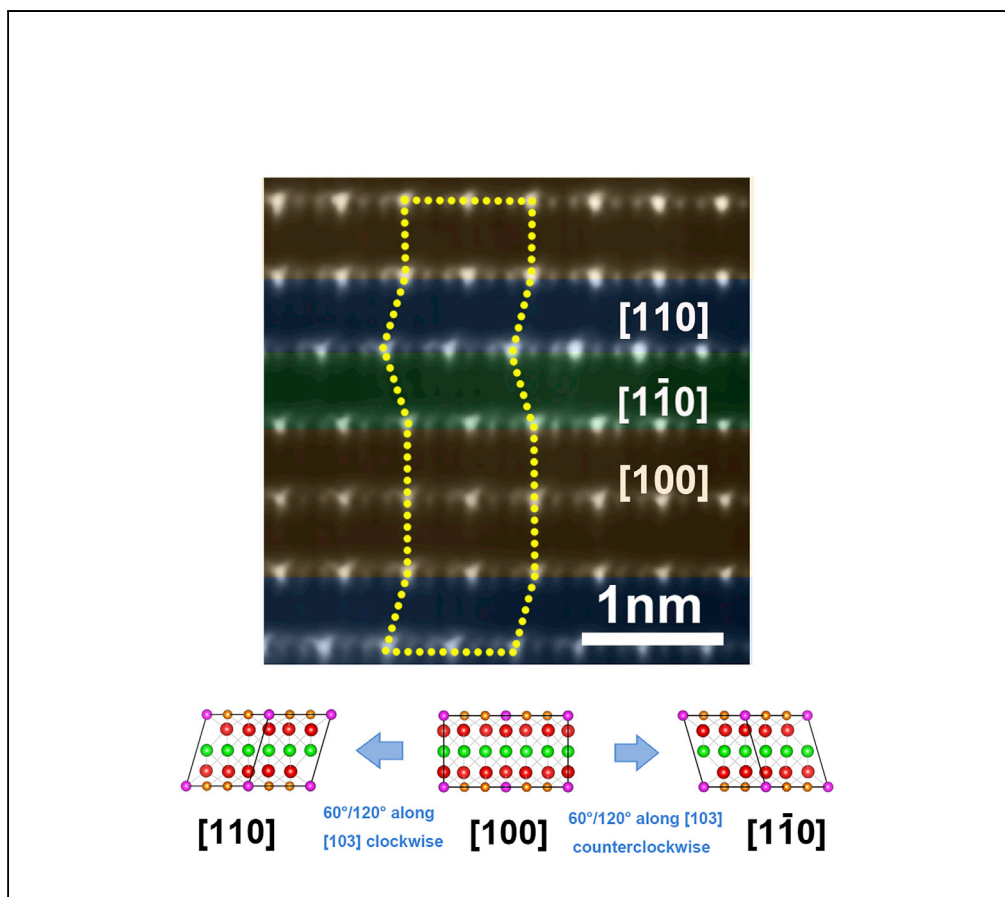**Article**

Insight into the Structural Disorder in Honeycomb-Ordered Sodium-Layered Oxide Cathodes

Lei Xiao,
Zhengping Ding,
Cheng Chen, ...,
Qun Huang, Peng
Gao, Weifeng Wei

p-gao@pku.edu.cn (P.G.)
weifengwei@csu.edu.cn
(W.W.)

HIGHLIGHTS

The intrinsic structural
disorder in $Na_3Ni_2SbO_6$ is
unambiguously revealed

Detailed atomic-
resolution STEM imaging
and crystallography
analysis are conducted

The structural disorder is
associated with three
variants of a monoclinic
phase

Article

Insight into the Structural Disorder in Honeycomb-Ordered Sodium-Layered Oxide Cathodes

Lei Xiao,[1,4] Zhengping Ding,[2,4] Cheng Chen,[1] Zhen Han,[3] Peng Wang,[3] Qun Huang,[1] Peng Gao,[2,*] and Weifeng Wei[1,5,*]

SUMMARY

Honeycomb-layered phases $Na_3M_2XO_6$ (M = Ni, Cu, Co; X = Sb, Bietc.) have been intensively pursued as high-voltage and high-rate capability cathode materials for Na-ion batteries (NIBs), but the crystal structure is not well elucidated. Herein, structural analysis was conducted on pristine $Na_3Ni_2SbO_6$ material using electron microscopy and associated spectroscopies to reveal its crystallographic features. Experimental observations along multiple zone axes indicate that structural disorder is intrinsic in the pristine $Na_3Ni_2SbO_6$, characteristic of randomly stacked layers with three variants of monoclinic structure. Stacking disorder is demonstrated by the non-vertical relationship of adjacent Ni_2SbO_6 layers in [100] zone axis, the different Ni/Sb atomic arrangements in [010] zone axis, and the Ni/Sb random overlap in [001] zone axis. The insight on the structural disorder may inspire studies on their phase transformations upon cycling and provide some clues to potentially solve the voltage/capacity decay problems of these honeycomb-layered materials.

INTRODUCTION

Currently, with the rapid increase of lithium-ion battery (LIB) applications in portable devices and electric vehicles, the present lithium resources can hardly meet the growing global demand (Dunn et al., 2011; Hwang et al., 2017; Masquelier and Croguennec, 2013; Ong et al., 2011). To tackle this problem, sodium-ion batteries (NIBs) have been pursued as a promising alternative due to their low cost, abundant supply as well as the electrochemical similarities to LIBs (Hwang et al., 2017; Yabuuchi et al., 2014). Distinct from the common lithium layered oxides, different Na^+ coordination in prismatic and octahedral site leads to two different types of layered oxides—P2-type (prismatic) and O3-type (octahedral) —and both have been extensively explored as NIB cathode materials (Delmas and Hagenmuller, 1980; Han et al., 2015; Hwang et al., 2016a, 2016b; Yabuuchi et al., 2012). Although P2-type cathode materials can deliver a high discharge capacity of more than 190 mAh/g, the low initial Na content and poor cycling stability make them impractical to meet the demands of Na full-cells (Han et al., 2016; Kalluri et al., 2014; Kang et al., 2016; Wang et al., 2015, 2016). Therefore, O3-type excels P2 type due to the sufficient Na content when considered as an ideal Na^+ reservoir to realize a practical Na-ion battery (de Boisse et al., 2015; Guo et al., 2015; Yu et al., 2014).

Among these O3-type cathode materials, $NaNiO_2$ is a model intercalation material that possesses high operating voltage and theoretical capacity, but the irreversible phase transformation during the initial cycling leads to rapid capacity fading and poor cycling stability, hindering its practical application in NIBs (Huon Han et al., 2014; Wang et al., 2017a, 2017b; Wang et al., 2014). With this perspective, researchers have tried to introduce 1/3 Sb^{5+} cations substitution of Ni^{2+} to form the honeycomb-ordered $NaNi_{2/3}Sb_{1/3}O_2$ (Politaev et al., 2010; Seibel et al., 2013). Given the ionic radius and charge difference between Ni^{2+} and Sb^{5+}, the 2:1 ratio gives rise to a distinct ordered cation arrangement in the Ni_2SbO_6 layers where each SbO_6 octahedron is surrounded by six NiO_6 octahedrons, forming a honeycomb-ordered superstructure (Wang et al., 2018; Zvereva et al., 2015). The partial substitution of Ni by Sb enables the stable low valence state of Ni(+2), inducing an intense electrostatic repulsion between Ni^{2+} and Sb^{5+} as well as a promoted voltage profile (Wang et al., 2017a, 2017b; You et al., 2017; Yuan et al., 2014) and improved air and thermal stabilities of $Na_3Ni_2SbO_6$ material (Wang et al., 2019). Interestingly, the imperfection of honeycomb ordering that relates to the Ni_2SbO_6 layer stacking has been widely noticed, which is sensitive to the synthesis conditions (Dai et al., 2017; Liu et al., 2016; Ma et al., 2015) and similar to that reported in

[1]State Key Laboratory of Powder Metallurgy, Central South University, Changsha, Hunan 410083, People's Republic of China

[2]International Center for Quantum Materials, and Electron Microscopy Laboratory, School of Physics, Peking University, Beijing 100871, People's Republic of China

[3]National Laboratory of Solid State Microstructures, College of Engineering and Applied Sciences, and Collaborative Innovation Center of Advanced Microstructures, Nanjing University, Nanjing, Jiangsu 210093, People's Republic of China

[4]These authors contributed equally

[5]Lead Contact

*Correspondence:
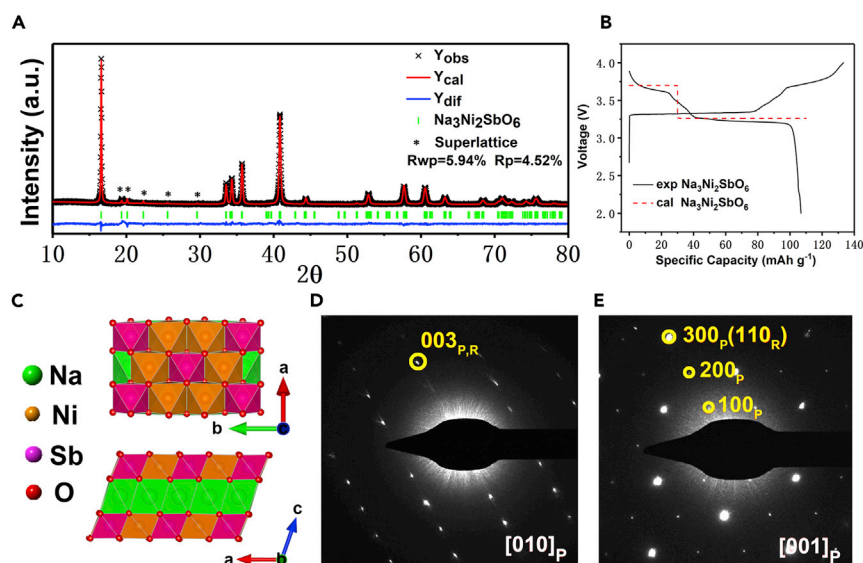p-gao@pku.edu.cn (P.G.),
weifengwei@csu.edu.cn
(W.W.)

https://doi.org/10.1016/j.isci.2020.100898

Figure 1. Preliminary Characterization of Na₃Ni₂SbO₆ Material

(A) The X-ray diffraction (XRD) pattern and Rietveld plot of pristine $Na_3Ni_2SbO_6$ material.

(B) Calculated and experimental voltage platform of $Na_3Ni_2SbO_6$.

(C) Crystal structure models of $Na_3Ni_2SbO_6$ viewed in [001] zone axis (top) and [010] zone axis (bottom).

(D) and (E) Selected area electron diffraction (SAED) patterns taken from the $Na_3Ni_2SbO_6$ material along the $[010]_P$ and $[001]_P$ zone axes respectively. "R" subscript indicates $R\bar{3}m$ space group and "P" subscript indicates $P3_112$ space group.

lithium-rich layered oxides (Zhao et al., 2020; Shukla et al., 2015), but the crystallographic characteristics of this structural disorder is still ambiguous.

Direct imaging of this honeycomb disordering at the atomic scale is crucial to correlate the structure and electrochemical performance in these materials. Here we apply atomic-resolution scanning transmission electron microscopy (STEM) to explicitly understand the in-plane honeycomb-ordering of Ni and Sb atoms in the Ni_2SbO_6 layers and the stacking disorder of Ni_2SbO_6 layers along c-axis in pristine $Na_3Ni_2SbO_6$ material. We discover that the structural disorder is a result of random stacking of the Ni_2SbO_6 layers with three different orientations along the c-axis, which generates disordered sequences and the overlap of Ni/Sb atoms that are evidenced by atomic-resolution STEM images in different zone axes.

RESULTS

The stoichiometric $Na_3Ni_2SbO_6$ material, as confirmed by inductively coupled plasma-optical emission spectrometry (ICP-OES) analysis (Table S1) and X-ray photoelectron spectroscopy (XPS) results (Figure S1), was synthesized via a simple solution combustion method. Typical scanning electron microscopy (SEM) image, high angle annular dark field image (HAADF-STEM) images, and corresponding energy dispersive X-Ray spectroscopy (EDX) elemental mappings demonstrate its plate-like morphology and uniform element distribution (Figure S2). Figure 1A and Tables S2 show the X-Ray diffraction (XRD) pattern and Rietveld refinement of pristine $Na_3Ni_2SbO_6$ material with all diffraction peaks that can be well indexed to a monoclinic $C2/m$ structure, as schematically illustrated in Figure 1C. The weak diffraction peaks located at 18–32° 2θ angles represent the honeycomb Ni/Sb ordering superstructure within ab plane (Viciu et al., 2007; Zvereva et al., 2012), where each SbO_6 octahedron is surrounded by six NiO_6 edge-sharing octahedron in the Ni_2SbO_6 planes (Wang et al., 2018). The experimental electrochemical cycle (Figure 1B) shows good agreement with calculated characteristic voltage profiles (Liu et al., 2016; Ma et al., 2015; Wang et al., 2019). The selected area electron diffraction (SAED) patterns in [010] and [001] zone axes were collected to provide information on in-plane honeycomb order and out-of-plane stacking disorder (Figures 1D and 1E). Extra streaks and varying degrees of scattering are observed in Figure 1D as the characteristics of stacking disorder along c-axis, indicating the deviation from ordered monoclinic stacking sequence along c-axis (Liu et al., 2016; Meng et al., 2005). As shown in Figure 1E, the simple $R\bar{3}m$ rhombohedral cell is inadequate for describing the SAED patterns collected in $[001]_R$ zones, whereas all observed diffraction spots can be well indexed by the $\sqrt{3} \times \sqrt{3} \times 1$ $P3_112$ trigonal
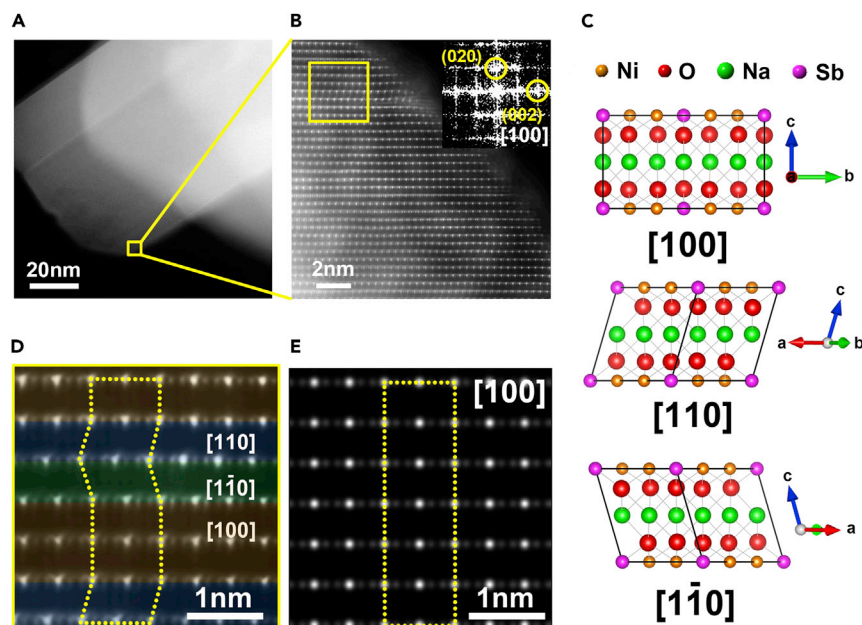
Figure 2. Structural Analysis along [100] Zone Axis

(A and B) (A) A low-magnification image and (B) corresponding magnified HAADF-STEM image of $Na_3Ni_2SbO_6$ at the [100] zone axis.

(C) Structure models showing the [100], [110], and [1$\bar{1}$0] projections, respectively.

(D) Colour-coded HAADF-STEM image showing the random distribution of the [100], [110], and [1$\bar{1}$0] projections.

(E) Simulated HAADF-STEM image along the [100] zone axis, showing perfect alignments of Ni and Sb atoms.

supercell, illustrating the existence of in-plane honeycomb-ordered superstructure (Ma et al., 2015). For $Na_3Ni_2SbO_6$ material, most investigations claimed that stacking disorder is induced by lateral displacement of the TM layers (Mortemard de Boisse et al., 2016; Wang et al., 2019), yet the explicit atomic-scale structure analysis considering different crystal orientations is scarce.

To have a deeper insight into the stacking relationship between layers, detailed atomic-resolution structural characterization of $Na_3Ni_2SbO_6$ material in [100] zone axis was performed. Figures 2A and 2B show the representative low-magnification and atomic-resolution HAADF-STEM images and fast Fourier transform (FFT) pattern. The bright spots and the relatively darker spots correspond to the Sb and Ni columns, respectively, showing the Sb–Ni–Ni–Sb sequence along b-axis (Lu et al., 2014). In principle, a perfect ordered monoclinic stacking sequence, viewed in the [100] zone axis, exhibits the same Ni and Sb atomic positions along c-axis, as shown in the first crystal model of Figure 2C. In the honeycomb-ordered superstructure that one SbO_6 octahedron is surrounded by six NiO_6 octahedrons in ab plane, the Ni_2SbO_6 layer overlaps after each rotation of 60° given the Sb site as the center of symmetry. Therefore, only three different crystal variants exist in ab plane, including [100], [110], and [1$\bar{1}$0] projections, as shown in Figure 2C. Evidently, projections corresponding to [100], [110], and [1$\bar{1}$0] zone axes of the monoclinic phase are observed and distinguished by orange, green, and blue bars in the enlarged STEM image (Figure 2D), which deviate from the perfect vertical alignment of Ni and Sb atoms in the simulated HAADF-STEM image along the [100] zone axis (Figure 2E). Based on the crystal orientation relationships between [100], [110], and [1$\bar{1}$0] zone axes, [100] can directly convert to [110] or [1$\bar{1}$0] by virtue of rotating 60° clockwise or counterclockwise in ab plane (Figure S3A), suggesting that the stacking disorder in pristine $Na_3Ni_2SbO_6$ material may originate from the rotation of ordered monoclinic Ni_2SbO_6 layers. This new observation differs from the stacking fault mechanism that was proposed in previous studies, involving the insertion and removal of layers and the deconstruction of ABC close-packed sequences (Aidhy et al., 2016; Ma et al., 2015).

To verify whether the stacking disorder is induced by rotation of the Ni_2SbO_6 layers, it is necessary to check the projections in other orientations. Figure 3A exhibits a representative HAADF-STEM image taken from the $Na_3Ni_2SbO_6$ material tilted to the [010] zone axis. Interestingly, two different projections of monoclinic
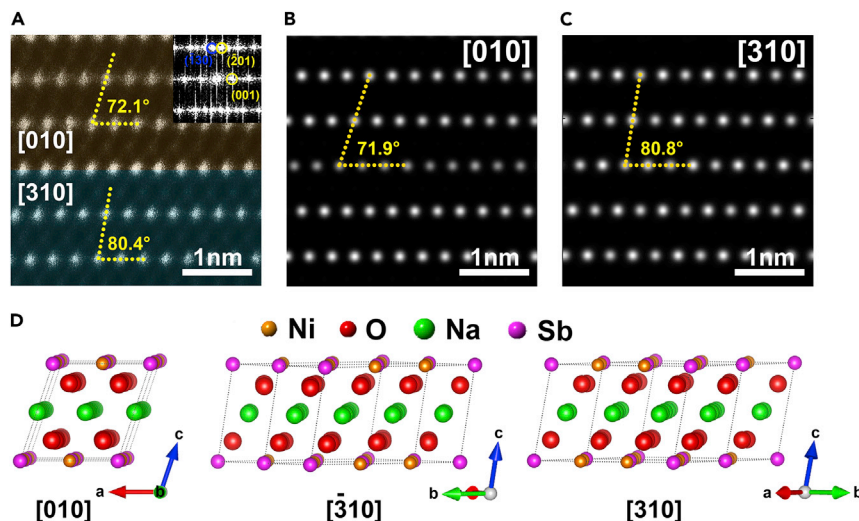
Figure 3. Structural Analysis along [010] Zone Axis

(A) Typical HAADF-STEM image and corresponding FFT pattern of $Na_3Ni_2SbO_6$ material along [010] zone axis.

(B and C) Simulated HAADF-STEM images of $Na_3Ni_2SbO_6$ material in [010] and [310]/[$\overline{3}$10] zone axes showing different atomic arrangements.

(D) Crystal models of the [010], [$\overline{3}$10], and [310] zone axes.

phase present in the same field of view are distinguished using different color bars, showing different measured angles (72.1° and 80.4°) for ABC stacking sequences (Figure 3A). The atomic arrangements of these two projections are well consistent with the simulated HAADF-QSTEM images along [010] and [310]/[$\overline{3}$10] zone axes (Figures 3B and 3C). The [310] and [$\overline{3}$10] zone axes show the same atomic distribution, making them indistinguishable in the HAADF-STEM image. As depicted schematically in Figure 3D, the atomic arrangements corresponding to [010], [$\overline{3}$10], and [310] orientations will fully overlap after 60 degrees of rotation, which further confirm that the stacking disorder is caused by the rotation of the Ni_2SbO_6 layers (Figure S3B).

The two directions that are parallel to *ab* plane show the existence of different variants of monoclinic phase via the rotation of Ni_2SbO_6 layers in the $Na_3Ni_2SbO_6$ material (Figures 2 and 3), but the interpretation of STEM images taken in the direction vertical to *ab* plane is still ambiguous in the literature. Figure 4A shows an HAADF-STEM image and corresponding FFT pattern in the [001] zone axis. In contrast, unlike those shown in the other two orientations, the atomic arrangements in the [001] zone axis exhibit a perfect honeycomb or hexagon pattern. The in-plane honeycomb structure indicates a single variant of monoclinic phase at first glance. It is worth noting that, however, uniform spot contrast that corresponds to Ni and
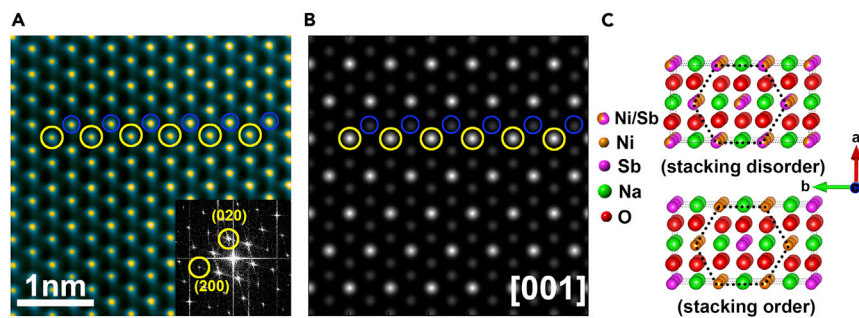

Figure 4. Structural Analysis along [001] Zone Axis

(A) HAADF-STEM image of $Na_3Ni_2SbO_6$ at [001] zone axis. Inset: FFT pattern.

(B) Simulated HAADF-STEM image of $Na_3Ni_2SbO_6$ material in [001] zone axis.

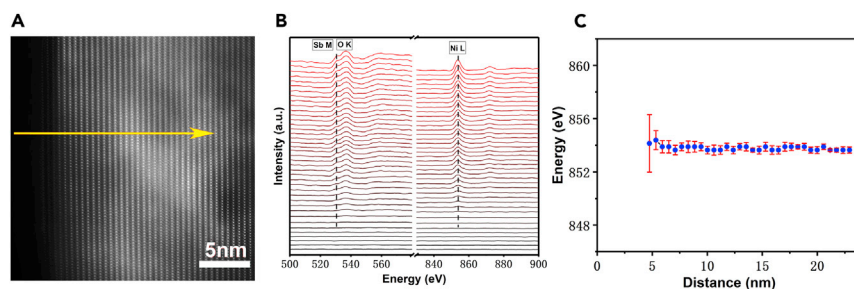(C) The corresponding model structure of stacking disorder and stacking order.

Figure 5. EELS Analysis of Na₃Ni₂SbO₆ Material

(A) HAADF-STEM image along [010] zone axis showing electron energy loss spectroscopy (EELS) spectrum taken from the horizontal yellow arrow.

(B) Corresponding EELS spectra for O K-, Ni L-, and Sb M-edges.

(C) Corresponding energy profile of Ni L₃ edge from the surface to the bulk.

Sb atoms can be observed in the HAADF-STEM image, which is in contradiction to the perfect honeycomb-ordered structure. The honeycomb-ordered arrangement of Ni and Sb atoms in *ab* plane can be seen in the simulated HAADF-STEM image (Figure 4B), where the brighter spots represent Sb atoms and the darker spots represent Ni atoms (marked by yellow open circle and blue open circle, respectively). The observed honeycomb-disordered structure (Figure 4A) can be ascribed to random overlap of Ni and Sb atoms in each column when viewed along *c*-axis, as illustrated schematically in Figure 4C. This Ni/Sb overlap feature is achieved by the rotation of some Ni_2SbO_6 layers, due to the six-fold overlap feature of the Ni_2SbO_6 layers in monoclinic structure (Figure S3C). In a word, the stacking disorder is demonstrated by the non-vertical relationship of adjacent Ni_2SbO_6 layers in [100] zone axis, the different Ni/Sb atomic arrangements in [010] zone axis, and the Ni/Sb random overlap in [001] zone axis.

To appreciate the chemical states of O/Ni/Sb ions across different Ni_2SbO_6 layers, atomic-resolution electron energy loss spectroscopy (EELS) line-scan analysis was also conducted on the pristine $Na_3Ni_2SbO_6$ material. Figure 5A shows an HAADF-STEM image with the EELS line-scan ranging from the surface to the bulk along the [010] zone axis. The corresponding O K-, Ni L-, and Sb M-edges spectra were plotted in Figure 5B. The energy loss peaks of O^{2-}, Ni^{2+}, and Sb^{5+} locate at the same position without noticeable chemical shift (Figures 5B and 5C), implying uniform chemical environments from the surface to $Na_3Ni_2SbO_6$ bulk. Based on the three-dimensional crystallographic evidence from HAADF-STEM images in various zone axes and chemical information from EDS- and EELS-STEM results, it is reasonable to conclude that the pristine $Na_3Ni_2SbO_6$ material is consisted of a single monoclinic phase, and the intrinsic structural disorder is associated with three different crystallographic variants.

DISCUSSION

In summary, we unambiguously unravel the intrinsic structure disorder in pristine honeycomb-ordered $Na_3Ni_2SbO_6$ material by means of electron microscopy and associated spectroscopy. We discover that the structural disorder is associated with three different crystallographic variants of a single monoclinic phase, showing in-plane honeycomb structure and out-of-plane stacking disorder induced by the rotation of Ni_2SbO_6 layers in *ab* plane. We anticipate that the insight on pristine honeycomb-ordered layered oxides would suggest new clues to researchers exploring the phase transitions occurred in this kind of materials upon cycling and potentially solving their voltage fading and capacity loss issues.

Limitations of the Study

We believe that the structural disorder is a result of random stacking of the Ni_2SbO_6 layers with three different orientations along the *c*-axis, which is also applicable to other honeycomb-ordered oxide material, such as $Na_3Ni_2BiO_6$, $Na_3Mg_2SbO_6$, and Na_2RuO_3, etc. However, direct atomic-resolution HAADF-STEM images of them are lacking. Meanwhile, the relationship between the structure and phase transformation is still unrevealed, and some structure analysis on the materials upon cycling is also lacking.

METHODS

All methods can be found in the accompanying Transparent Methods supplemental file.

iScience

CellPress

AUTHOR CONTRIBUTIONS

W.W. and P.G. conceived the idea and directed the research. L.X. and Q.H. performed the material synthesis, SEM, and XRD analysis of the sample. Z.D., W.W., and P.G. performed the STEM measurements and analyzed the STEM results. C.C., Z.H., and P.W. performed quantitative-STEM (QSTEM) simulations. W.W. and L.X. co-wrote the manuscript and all authors discussed the results and made comments on the manuscript.

DECLARATION OF INTERESTS

The authors declare no competing interests.

REFERENCES

Aidhy, D.S., Lu, C., Jin, K., Bei, H., Zhang, Y., Wang, L., and Weber, W.J. (2016). Formation and growth of stacking fault tetrahedra in Ni via vacancy aggregation mechanism. Scripta Mater. *114*, 137–141.

de Boisse, B.M., Cheng, J.H., Carlier, D., Guignard, M., Pan, C.J., Bordere, S., Filimonov, D., Drathen, C., Suard, E., Hwang, B.J., et al. (2015). O3-NaxMn1/3Fe2/3O2 as a positive electrode material for Na-ion batteries: structural evolutions and redox mechanisms upon Na+ (de) intercalation. J. Mater. Chem. A *3*, 10976–10989.

Dai, H., Yang, C., Ou, X., Liang, X., Xue, H., Wang, W., and Xu, G. (2017). Unravelling the electrochemical properties and thermal behavior of NaNi2/3Sb1/3O2 cathode for sodium-ion batteries by in situ X-ray diffraction investigation. Electrochim. Acta *257*, 146–154.

Delmas, C.F., and Hagenmuller, P. (1980). Structural classification and properties of the layered oxides. Phys. B+C *99*, 81–85.

Dunn, B., Kamath, H., and Tarascon, J.M. (2011). Electrical energy storage for the grid: a battery of choices. Science *334*, 928–935.

Guo, H., Wang, Y., Han, W., Yu, Z., Qi, X., Sun, K., Hu, Y.-S., Liu, Y., Chen, D., and Chen, L. (2015). Na-deficient O3-type cathode material Na-0.8 Ni0.3Co0.2Ti0.5 O-2 for room-temperature sodium-ion batteries. Electrochim. Acta *158*, 258–263.

Han, M.H., Gonzalo, E., Singh, G., and Rojo, T. (2015). A comprehensive review of sodium layered oxides: powerful cathodes for Na-ion batteries. Energy Environ. Sci. *8*, 81–102.

Han, M.H., Gonzalo, E., Sharma, N., Lopez delAmo, J.M., Armand, M., Avdeev, M., Garitaonandia, J.J.S., and Rojo, T. (2016). High performance P2-phase Na2/3Mn0.8Fe0.1Ti0.1O2 cathode material for ambient-temperature sodium-ion batteries. Chem. Mater. *28*, 106.

Huon Han, M., Gonzalo, E., Casas-Cabanas, M., and Rojo, T. (2014). Structural evolution and electrochemistry of monoclinic NaNiO2 upon the first cycling process. J. Power Sources *258*, 266–271.

Hwang, J.-Y., Myung, S.-T., Yoon, C.S., Kim, S.-S., Aurbach, D., and Sun, Y.-K. (2016a). Novel cathode materials for Na-ion batteries composed of spoke-like nanorods of Na Ni0.61Co0.12Mn0.27 O-2 assembled in spherical secondary particles. Adv. Funct. Mater. *26*, 8083–8093.

Hwang, J.-Y., Belharouak, I., and Sun, Y.-K. (2016b). A comprehensive study of the role of transition metals in O3-type layered Na [NixCoyMnz]O2 (x 1/3, 0.5, 0.6, and 0.8) cathodes for sodium-ion batteries. J. Mater. Chem. A *4*, 17952–17959.

Hwang, J.-Y., Myung, S.-T., and Sun, Y.-K. (2017). Sodium-ion batteries: present and future. Chem. Soc. Rev. *46*, 3529–3614.

Kalluri, S., Seng, K.H., Pang, W.K., Guo, Z., Chen, Z., Liu, H.-K., and Dou, S.X. (2014). Electrospun P2-type Na-2/3(Fe1/2Mn1/2)O-2 hierarchical nanofibers as cathode material for sodium-ion batteries. ACS Appl. Mater. Interfaces *6*, 8953–8958.

Kang, W., Yu, D.Y.W., Lee, P.-K., Zhang, Z., Bian, H., Li, W., Ng, T.-W., Zhang, W., and Lee, C.-S. (2016). P2-Type NaxCu0.15Ni0.20Mn0.65O2 cathodes with high voltage for high-power and long-life sodium-ion batteries. ACS Appl. Mater. Interfaces *8*, 31661–31668.

Liu, J., Yin, L., Wu, L., Bai, J., Bak, S.M., Yu, X., Zhu, Y., Yang, X.Q., and Khalifah, P.G. (2016). Quantification of honeycomb number-type stacking faults: application to Na3Ni2BiO6 cathodes for Na-ion batteries. Inorg. Chem. *55*, 8478–8492.

Lu, X., Wang, Y., Liu, P., Gu, L., Hu, Y.S., Li, H., Demopoulos, G.P., and Chen, L. (2014). Direct imaging of layered O3- and P2-NaxFe1/2Mn1/ 2O2 structures at the atomic scale. Phys. Chem. Chem. Phys. *16*, 21946–21952.

Ma, J., Bo, S.-H., Wu, L., Zhu, Y., Grey, C.P., and Khalifah, P.G. (2015). Ordered and disordered polymorphs of Na(Ni2/3Sb1/3)O2: honeycomb-ordered cathodes for Na-ion batteries. Chem. Mater. *27*, 2387–2399.

Masquelier, C., and Croguennec, L. (2013). Polyanionic (phosphates, silicates, sulfates) frameworks as electrode materials for

rechargeable Li (or Na) batteries. Chem. Rev. *113*, 6552–6591.

Meng, Y.S., Grey, C.P., Yoon, W.-S., Jiang, M., Bre'ger, J., and Shao-Horn, Y. (2005). Cation Ordering in Layered O3 Li[NixLi1/32x/3Mn2/3-x/3]O2(0 e x e 1/2) Compounds. Chem. Mater. *17*, 2386–2394.

Mortemard de Boisse, B., Liu, G., Ma, J., Nishimura, S.I., Chung, S.C., Kiuchi, H., Harada, Y., Kikkawa, J., Kobayashi, Y., Okubo, M., et al. (2016). Intermediate honeycomb ordering to trigger oxygen redox chemistry in layered battery electrode. Nat. Commun. *7*, 11397.

Ong, S.P., Chevrier, V.L., Hautier, G., Jain, A., Moore, C., Kim, S., Ma, X., and Ceder, G. (2011). Voltage, stability and diffusion barrier differences between sodium-ion and lithium-ion intercalation materials. Energy Environ. Sci. *4*, 3680–3688.

Politaev, V.V., Nalbandyan, V.B., Petrenko, A.A., Shukaev, I.L., Volotchaev, V.A., and Medvedev, B.S. (2010). Mixed oxides of sodium, antimony (5+) and divalent metals (Ni, Co, Zn or Mg). J. Solid State Chem. *183*, 684–691.

Seibel, E.M., Roudebush, J.H., Wu, H., Huang, Q., Ali, M.N., Ji, H., and Cava, R.J. (2013). Structure and magnetic properties of the alpha-NaFeO2-type honeycomb compound Na3Ni2BiO6. Inorg. Chem. *52*, 13605–13611.

Shukla, A.K., Ramasse, Q.M., Ophus, C., Duncan, H., Hage, F., and Chen, G. (2015). Unravelling structural ambiguities in lithium- and manganese-rich transition metal oxides. Nat. Commun. *6*, 8711.

Viciu, L., Huang, Q., Morosan, E., Zandbergen, H.W., Greenbaum, N.I., McQueen, T., and Cava, R.J. (2007). Structure and basic magnetic properties of the honeycomb lattice compounds Na2Co2TeO6 and Na3Co2SbO6. J. Solid State Chem. *180*, 1060–1067.

Wang, X., Liu, G., Iwao, T., Okubo, M., and Yamada, A. (2014). Role of ligand-to-metal charge transfer in O3-type NaFeO2-NaNiO2 solid solution for enhanced electrochemical properties. J. Phys. Chem. C *118*, 2970–2976.

Wang, Y., Xiao, R., Hu, Y.-S., Avdeev, M., and Chen, L. (2015). P2-Na-0.6 Cr0.6Ti0.4 O-2 cation-disordered electrode for high-rate symmetric rechargeable sodium-ion batteries. Nat. Commun. *6*, 6954.

Wang, P.-F., You, Y., Yin, Y.-X., Wang, Y.-S., Wan, L.-J., Gu, L., and Guo, Y.-G. (2016). Suppressing the P2-O2 phase transition of Na0.67Mn0.67Ni0.33O2 by magnesium substitution for improved sodium-ion batteries. Angew. Chem. Int. Ed. *55*, 7445–7449.

Wang, L., Zhang, X., Ren, Y., Zuo, P., Yin, G., and Wang, J. (2017a). Unravelling the origin of irreversible capacity loss in NaNiO2 for high voltage sodium ion batteries. Nano Energy *34*, 215–223.

Wang, P.-F., Guo, Y.-J., Duan, H., Zuo, T.-T., Hu, E., Attenkofer, K., Li, H., Zhao, X.S., Yin, Y.-X., Yu, X., et al. (2017b). Honeycomb-ordered Na3Ni1.5M0.5BiO6 (M = Ni, Cu, Mg, Zn) as high-voltage layered cathodes for sodium-ion batteries. ACS Energy Lett. *2*, 2715–2722.

Wang, P.-F., Yao, H.-R., You, Y., Sun, Y.-G., Yin, Y.-X., and Guo, Y.-G. (2018). Understanding the structural evolution and Na+ kinetics in honeycomb-ordered O'3-Na3Ni2SbO6 cathodes. Nano Res. *11*, 3258–3271.

Wang, P.F., Weng, M., Xiao, Y., Hu, Z., Li, Q., Li, M., Wang, Y.D., Chen, X., Yang, X., Wen, Y., et al. (2019). An ordered Ni6 -ring superstructure enables a highly stable sodium oxide cathode. Adv. Mater. *31*, e1903483.

Yabuuchi, N., Kajiyama, M., Iwatate, J., Nishikawa, H., Hitomi, S., Okuyama, R., Usui, R., Yamada, Y., and Komaba, S. (2012). P2-type Nax [Fe1/2Mn1/2]O2 made from earth-abundant

elements for rechargeable Na batteries. Nat. Mater. *11*, 512.

Yabuuchi, N., Kubota, K., Dahbi, M., and Komaba, S. (2014). Research development on sodium-ion batteries. Chem. Rev. *114*, 11636–11682.

You, Y., Kim, S.O., and Manthiram, A. (2017). A honeycomb-layered oxide cathode for sodium-ion batteries with suppressed P3-O1 phase transition. Adv. Energy Mater. *7*, 1601698.

Yu, H., Guo, S., Zhu, Y., Ishida, M., and Zhou, H. (2014). Novel titanium-based O-3-type NaTi0.5Ni0.5O2 as a cathode material for sodium ion batteries. Chem. Commun. (Camb.) *50*, 457–459.

Yuan, D., Liang, X., Wu, L., Cao, Y., Ai, X., Feng, J., and Yang, H. (2014). A honeycomb-layered Na3Ni2SbO6: a high-rate and cycle-stable cathode for sodium-ion batteries. Adv. Mater. *26*, 6301–6306.

Zhao, E., Wang, X., Hu, E., Liu, J., Yu, X., Olguin, M., Wynn, T.A., Meng, Y.S., Page, K., Wang, F., et al. (2020). Local structure adaptability through multi cations for oxygen redox accommodation in Li-Rich layered oxides. Energy Storage Mater. *24*, 384–393.

Zvereva, E.A., Evstigneeva, M.A., Nalbandyan, V.B., Savelieva, O.A., Ibragimov, S.A., Volkova, O.S., Medvedeva, L.I., Vasiliev, A.N., Klingeler, R., and Buechner, B. (2012). Monoclinic honeycomb-layered compound Li3Ni2SbO6: preparation, crystal structure and magnetic properties. Dalton Trans. *41*, 572–580.

Zvereva, E.A., Stratan, M.I., Ovchenkov, Y.A., Nalbandyan, V.B., Lin, J.Y., Vavilova, E.L., Iakovleva, M.F., Abdel-Hafiez, M., Silhanek, A.V., Chen, X.J., et al. (2015). Zigzag antiferromagnetic quantum ground state in monoclinic honeycomb lattice antimonatesA3Ni2SbO6(A=Li,Na). Phys. Rev. B *92*, 144401.

Supplemental Information

Insight into the Structural Disorder

in Honeycomb-Ordered

Sodium-Layered Oxide Cathodes

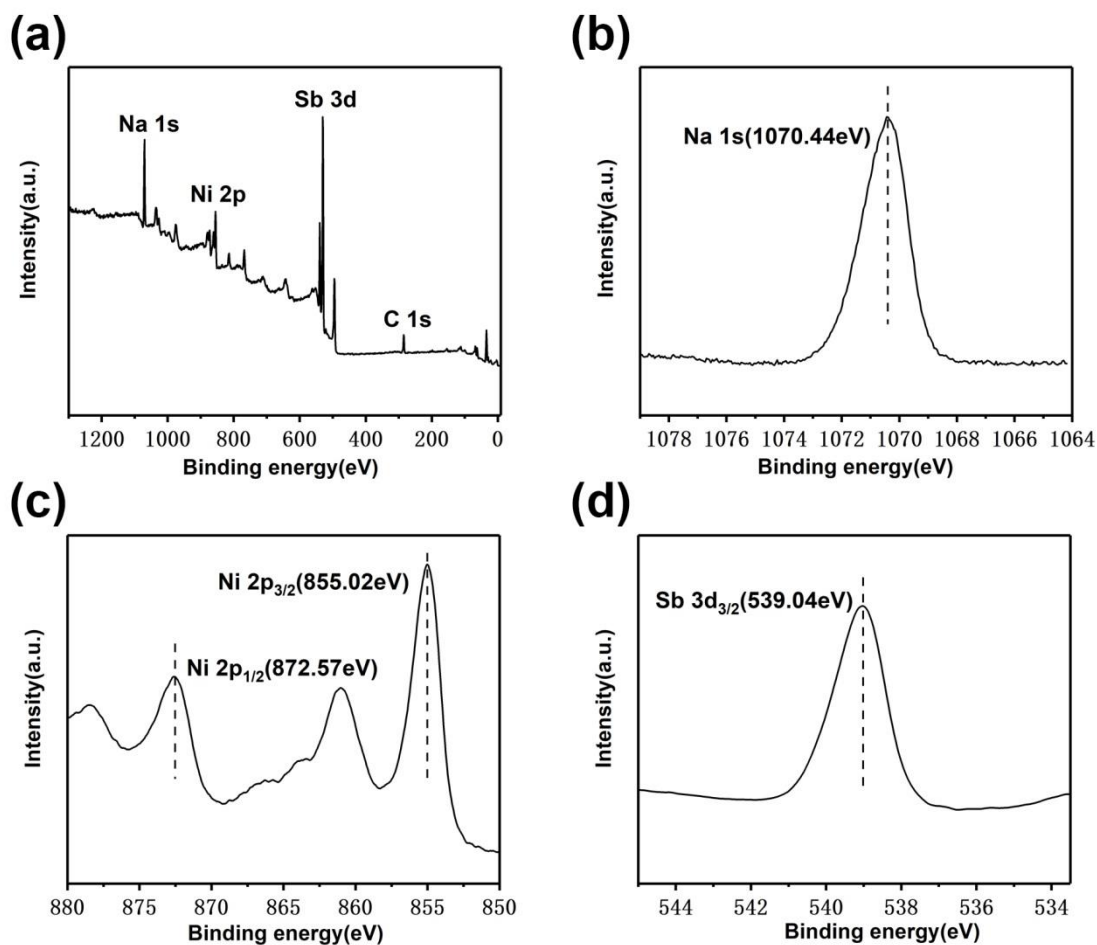Lei Xiao, Zhengping Ding, Cheng Chen, Zhen Han, Peng Wang, Qun Huang, Peng Gao, and Weifeng Wei

Figure S1. (a) XPS full survey spectrum of $Na_3Ni_2SbO_6$ material. (b)-(d) High resolution XPS spectra of the (b) Na 1s, (c) Ni 2p, and (d) Sb 3d. Related to Figure 1.

Figure S1 shows XPS results of $Na_3Ni_2SbO_6$ material. Ni^{2+} is confirmed in the pristine electrode as evidenced by the main peak at 855.0 eV and the satellite peak at 862.2 eV in $Ni-2p_{3/2}$ spectra as well as the peak at 872.6ev in $Ni-2p_{1/2}$ spectra.(Wang et al., 2018) The Na 1s peak (Figure S1b) and Sb $3d_{3/2}$ peak (Figure S1d) were centered at binding energy of 1,070.44 eV and 539.04eV, respectively, indicating the +1 and +5 oxidation state of sodium and antimony.
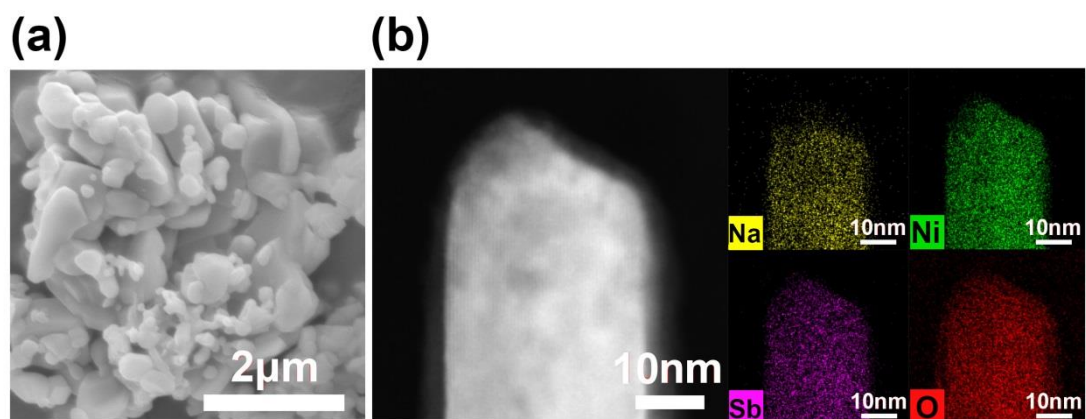
Figure S2. (a) SEM image of the pristine $Na_3Ni_2SbO_6$ material. (b) HAADF-STEM image and the corresponding EDX elemental mappings of Na, Ni, Sb and O of the pristine $Na_3Ni_2SbO_6$ material. Related to Figure 1.

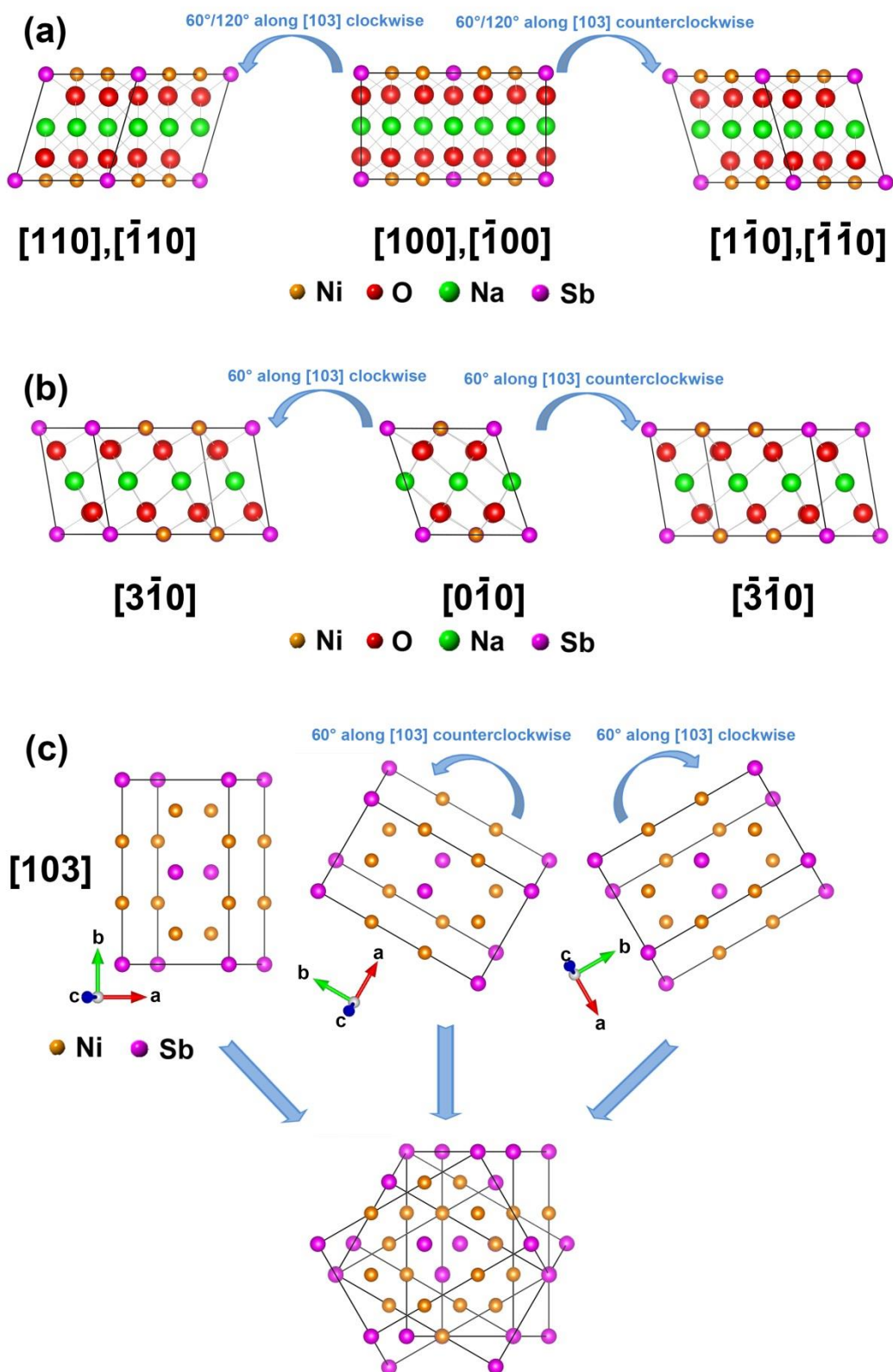**Figure S3**. Schematic diagram of rotation symmetry of the pristine $Na_3Ni_2SbO_6$ structure in different orientations. Related to Figure 2-4.

Table S1. ICP analysis of $Na_3Ni_2SbO_6$ sample. Related to Figure 1.

Sample	Na	Ni	Sb
$Na_3Ni_2SbO_6$	2.97	1.98	1.02

Table S2. Structural parameters determined from the Rietveld refinement of the XRD data for $Na_3Ni_2SbO_6$ sample. Related to Figure 1.

Atom	x	y	z	Occ.
Na1	0	0.5	0.5	1
Na2	0.5	0.349922	0.5	1
Ni1	0	0.662319	0	0.8191
Ni2	0	0	0	0.3618
Sb1	0	0	0	0.638
Sb2	0	0.662959	0	0.1809
O1	0.236934	0.831315	0.199014	1
O2	0.211618	0.5	0.204429	1
a=5.3146 Å	b=9.2013 Å	c=5.6348 Å	R_p=4.09%	R_{wp}=5.43%

Transparent Methods

Material synthesis: The $Na_3Ni_2SbO_6$ material was prepared via a simple solution combustion with stepwise high-temperature solid-state method. Stoichiometric amounts of $NaNO_3$, $Ni(CH_3COO)_2$, $Sb(CH_3COO)_3$ and glucose were firstly dissolved in deionized water. The precursor solution was evaporated to a gel in a water bath at 80 ℃. Then, the gel was transferred to a crucible and heated to 250 ℃ to ignite it. The combustion product was collected and ground into powder using a mortar. Finally, the powder was calcined in muffle furnace at 800 ℃ for 15h in air atmosphere. After sintering, the as-prepared $Na_3Ni_2SbO_6$ material was transferred into a glove box with argon-filled atmosphere to protect the material from moisture and CO_2.

Electrochemical Characterizations: The electrochemical measurements of the pristine $Na_3Ni_2SbO_6$ cathode were carried out using CR2016 coin half-cells. The electrode for testing was fabricated by blending the active materials, acetylene black and polyvinylidene fluoride (PVDF) binder in a weight ratio of 8:1:1 in N-methyl-2-pyrrolidone (NMP). The obtained slurry was magnetically stirred for 1h and then pasted onto aluminum foil homogeneously and dried at 110 ℃ for 12 h in a vacuum oven. Then the coated foil was punched and the corresponding active material loading into circular pieces of 12.5 mm in diameter on each piece was approximately 2 mg. Coin-type half-cells were assembled in an Ar-filled glove box (MBraun, Germany) by using the as-prepared electrode pieces as the cathode, metallic sodium as the counter and reference electrode, glass fiber (DF-F) as the separator and 1 M $NaPF_6$ in ethylene carbonate (EC)/dimethyl carbonate (DEC) (1:1, v/v) with 3 vol%

fluoroethylene carbonate (FEC) as an additive as the electrolyte. The charge/discharge tests were performed using a Land cell test system at room temperature, in the range of 2V-4V (vs. Na^+/Na).

Morphological, Structural and Elemental Characterizations: The chemical composition was determined using inductively coupled plasma-atomic emission spectrometry (ICP-AES). The average crystallographic structure of the as-prepared $Na_3Ni_2SbO_6$ material was analyzed by X-ray diffraction (XRD, Bruker D8 ADVANCE, Germany) with Cu Ka radiation and a step size of 0.02 ° at a dwell time of 2s. Rietveld refinement of the XRD data was completed by General Structure Analysis System (GSAS) software. The morphology of the samples was observed with field emission scanning electron microscopy (SEM, FEG250, FEI QUANTA). The chemical states of the elements were evaluated by X-ray photoelectron spectroscopy (XPS) (ESCALAB 250Xi, Thermo Scientific, USA). High-resolution TEM images, SEAD patterns and STEM HAADF images were carried out on an aberration-corrected FEI (Titan Cubed Themis G2) equipped with an X-FEG gun at 300 kV. The beam current was ~50 pA, the convergence semiangle was 30 mrad, and a collection semi-angle snap was in the range of 80-379 mrad. The STEM-EDX mapping are obtained with a beam current of ~100pA and counts ranging from 1k cps to 3k cps for ~15 min with a Bruker Super-X EDS four-detector. All electron energy loss spectroscopy (EELS) spectra were acquired on a Gatan Enfinium ER 977 system. The EELS data was acquired at the collection semi-angle of 5.9 mrad, the convergence semi-angle of 25 mrad and a dispersion of 0.25 eV/ch. All simulated

STEM-HAADF images were acquired by QSTEM software, and all crystal structures were extended to 70~90 nm along the electron beam incident direction. The simulation parameters are consistent with the actual STEM experiments.

Supplemental References

Wang, P.-F., Yao, H.-R., You, Y., Sun, Y.-G., Yin, Y.-X., and Guo, Y.-G. (2018). Understanding the structural evolution and Na+ kinetics in honeycomb-ordered O'3-Na3Ni2SbO6 cathodes. Nano Research *11*, 3258-3271.